Localized surface plasmon resonance effect of bismuth nanoparticles in Bi/TiO2 catalysts for boosting visible light-driven CO2 reduction to CH4

Wenjie He [a,b], Jing Xiong [a], Zhiling Tang [a], Yingli Wang [a], Xiong Wang [a], Hui Xu [c], Zhen Zhao [a], Jian Liu [a], Yuechang Wei [a,*]

[a] State Key Laboratory of Heavy Oil Processing, Key Laboratory of Optical Detection Technology for Oil and Gas, China University of Petroleum, Beijing 102249, China
[b] Chongqing College of Electronic Engineering, Chongqing 401331, China
[c] Institute for Energy Research, Jiangsu University, Zhenjiang 212013, China

ARTICLE INFO

ABSTRACT

Herein, the photocatalysts of metallic Bi-modified TiO2 microsphere (namely BTO) were synthesized by one-pot solvothermal method. The localized surface plasmon resonance (LSPR) effect of introduced metallic Bi nanoparticles is beneficial to improve the absorption efficiency for visible light, and its surface hot electrons can donate to the valence band of TiO2 for boosting the separation efficiency of light generated electron-hole pairs. BTO catalysts exhibit the super catalytic activity for visible light-driven CO2 reduction with H2O to CH4. The formation amount and selectivity of CH4 product over BTO-2 catalyst are 49.12 μmol g^{-1} and 85.48 % for 4 h, respectively. Based on the results of in-situ DRIFTS and density functional theory calculation, the mechanism for photocatalytic CO2 reduction is proposed: the visible light-driven LSPR effect on BTO catalyst can boost the key step of CO2* -to-HCO* for promoting selective generation of CH4 product. It inspires the design of efficient photocatalysts for CO2 conversion.

1. Introduction

The overutilization of primary energy has caused a large emission of greenhouse gas, which has led to a great burden on the Earth's environment. Hence, scientists around the world are working to reduce the emission of carbon dioxide, as well as developing technologies for carbon dioxide capture, use and storage [1–3]. Photocatalysis, as a green and sustainable technology, has been widely studied since the second half of the last century [4–9], in which the use of solar energy to convert carbon dioxide and water into higher calorific value compounds has become a research hotspot of carbon dioxide recycling in the recent decade [10–17]. However, the development of light-driven redox technology still faces to barriers, such as low light utilization, low reaction efficiency, and unclear reaction mechanism. Hence, it is very significant to design and synthesis efficient photocatalysts, especially to investigate the structure-activity relationship between properties and mechanisms [18–21]. Moreover, the C═O bond in carbon dioxide with high dissociation energy of ~750 kJ mol^{-1} could be an enormous challenge to break. Thus, a large number of energetic hot electrons with a more negative redox potential need to be injected to destroy the intramolecular equilibrium [22–25]. The modification of semiconductor materials with inherent negative conduction band position is a crucial prerequisite for the development of new photocatalytic CO2 reduction catalysts.

Titanium dioxide (TiO2), the most widely studied photocatalyst, is also eye-catching research on catalysts for CO2 conversion because of its relatively negative and adjustable conduction band position [26–29]. But the nonresponse to visible light and the rapid electron-hole pairs recombination have limited its further application extremely. In this regard, some strategies are frequently employed to introduce cocatalysts for improving the light absorption and carrier mobility of catalysts, such as, heterojunction establishment, surface modification (ions doping and surface loading), and so on [30–34]. The cocatalysts (electron and hole types) are usually introduced into the catalytic system as active components and directly participate in the adsorption activation of the reactants. The special properties of cocatalyst could be utilized to functionalize the support material for improving its performance. The migration of the photogenerated charge to the cocatalyst could further inhibit the recombination of photogenerated electron-hole pairs and the reverse reaction between the active species and the products in the

---

reaction process. The cocatalyst can accelerate the reaction and consume the photogenerated carriers, especially the holes, which avoids the photocorrosion oxidation of the photocatalytic system and improves the stability of the photocatalytic system. Thus, to improve the light absorption property of the TiO_2 based catalysts and increase the carrier density of the catalysis system, noble metals as electron-type cocatalysts are often introduced by researchers due to their localized surface plasmon resonance effect [35–38]. The reported 0D/2D Au/TiO_2 materials with LSPR effect contributed to the light absorption, resulting in an excellent photocatalytic activity of CO_2 reduction to CH_4 [39]. And the Ag modified TiO_2 supported by the LSPR effect has exhibited excellent photocatalytic activity for CO_2 reduction [40]. It is worth noting that non-noble metallic Bi also possesses the localized surface plasmon resonance effect, and is often introduced to modify the photoelectric properties of catalysts [41–45]. The simultaneous addition of the Bi source and reducing agent during TiO_2 synthesis will simplify the modification process of the composite catalyst, and the in-situ loading method can form a stronger interaction between metallic Bi and TiO_2 support, which facilitates the transfer of charge carriers between them.

In this work, the non-noble metallic Bi nanoparticles were employed to couple with spherical TiO_2 material by the one-pot solvothermal method. The metallic Bi nanoparticles with recognized LSPR effect, can not only improve the light absorption range of spherical TiO_2 catalyst to the visible spectrum, but also inhibit the recombination of light induced electron-hole pairs. The highly efficient separation of light induced electron-hole pairs promoted the migration of energetic hot electrons to the surface of TiO_2 catalyst. And the abundant adsorption of reactant CO_2 over metallic Bi modified TiO_2 catalyst was assisted by the enriched surface photoelectrons. Based on the results of in-situ DRIFTS and DFT calculation, the loading of metallic Bi nanoparticles on the spherical TiO_2 surface are beneficial to boost the dynamic production and consumption of •CO_2 species under the visible light irradiation condition, which reduces the reaction energy of CO* to HCO* species and promotes the photocatalytic CO_2 reduction to CH_4 product. This study provides an idea for the design and preparation of efficient photocatalysts and insight into the mechanism of catalytic reactions.

2. Experimental section

2.1. Preparation of Catalysts

All reagents used in the experiment are analytical grade and did not require further purification. The synthesis process of metallic bismuth-modified titanium dioxide (Bi-TiO_2) microsphere catalysts was conducted via a one-pot solvothermal method, as illustrated in Scheme 1. Initially, a Teflon liner (100 mL) was charged with isopropanol (35 mL) as the solvent. Triethylenediamine (20 mg) and a specific quantity of bismuth nitrate were then added to the isopropanol solvent, followed by magnetic stirring for 60 min. Subsequently, under the protection of an inert gas (N_2), tetrabutyl titanate (1.5 mL) was rapidly introduced into the aforementioned mixture, and magnetic stirring was continued for another 60 min. Finally, the Teflon liner, containing all the precursor reagents and secured within a stainless-steel reactor, was transferred to

an oven. The solvothermal reaction was carried out at a constant temperature of 180 °C for 20 h. The resulting precipitate was washed with absolute ethanol five times and subsequently dried in an oven at 60 °C for 12 h to obtain a gray powder. The metallic Bi-TiO_2 microsphere catalysts exhibited varying shades of gray, depending on the amount of bismuth resources added during the synthesis process (theoretical molar percentages of bismuth atoms in titania were 0.01 %, 0.05 %, and 0.20 % for BTO-1, BTO-2, and BTO-3, respectively). Notably, the BTO-2 catalyst, after calcination at 500 °C for 2 h, was denoted as BTO-2 C.

2.2. Characterizations

A comprehensive characterization of the synthesized metallic Bi modified TiO_2 microsphere catalysts was conducted using various advanced techniques. These included XRD, SEM, TEM, UV-Vis DRS, PL, CO_2-TPD, XPS, and so on. Detailed descriptions of these characterization techniques can be found in the Materials characterizations section of the Supporting Information.

### 2.3. Photocatalytic CO_2 reduction measurement

The photocatalytic efficiency of the synthesized catalysts in facilitating the conversion of CO_2 under visible light irradiation was assessed through rigorous gas-solid phase reactions (Scheme S1) conducted in the Labsolar-III equipment (Perfectlight Corp, China). This experimental setup involved the use of a Xenon lamp with a UV cutoff filter (420 nm) to ensure selective excitation. The comprehensive methodology and results of these investigations have been meticulously documented in the Supporting Information. The CO_2 photoreduction selectivity (Eq. (1)) and the CH_4 product selectivity (Eq. (2)) were quantitatively determined using the following mathematical expressions:

$$S_{CO_2} \quad (\%) = \frac{Mole \quad number \quad of (CH_4 \times 8 + CO \times 2)}{Mole \quad number \quad of (H_2 \times 2 + CH_4 \times 8 + CO \times 2)} \quad (1)$$

$$S_{CO_4} \quad (\%) = \frac{Mole \quad number \quad of \quad CH_4 \times 8}{Mole \quad number \quad of (CH_4 \times 8 + CO \times 2)} \quad (2)$$

2.4. In-situ DRIFTS measurement

In order to investigate the process of converting photocatalytic CO_2 into CO, in-situ diffuse reflectance infrared Fourier transform spectroscopy (in-situ DRIFTS) experiments were performed by using VERTEX 70 FTIR spectrometers (Bruker Corp, Germany). To eliminate the influence of external gases and remove any adsorbed impurities on the catalyst surface, the equipment system underwent vacuum treatment. Initially, a background spectrum was recorded and subtracted under vacuum conditions. Subsequently, the prepared materials were exposed to humid high-purity CO_2 at a pressure of 101.325 kPa, which contained 1 kPa of H_2O vapor. Finally, time-dependent DRIFTS spectra over the catalysts were recorded with and without light irradiation at 2-minute intervals, accumulating 32 scans per spectrum with a resolution of 4 cm^{-1} under room temperature conditions.
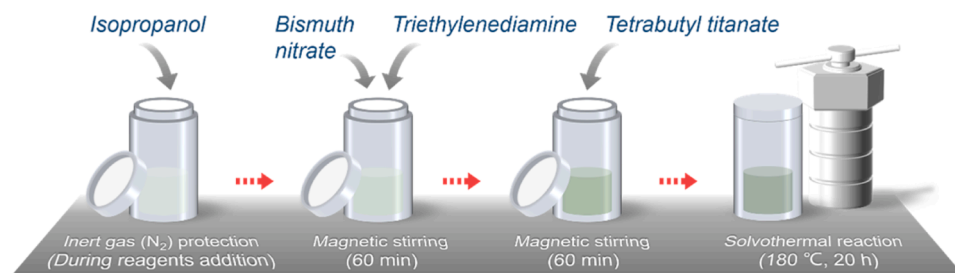
Scheme 1. The one pot solvothermal synthesis process of BTO catalysts.

2.5. Density functional theory calculation

The study utilized the "Vienna Ab Initio Simulation Package" (VASP code 5.4.1) and the generalized gradient correlation functional for spin-polarized density functional theory (DFT)-D2 calculations. The projector-augmented wave method with a plane-wave basis was implemented [46]. A cut-off energy of 400 eV and a Gaussian smearing width of 0.2 eV were employed. The Brillouin zone was sampled with $5 \times 5 \times$ K points. All structures and energies relaxing below 0.05 eV Å^{-1} were considered [47]. The adsorption energy (Eads) was determined as $E_{ads} = E_{tot} - (E_s + E_m)$, where E_{tot}, E_s, and E_m represent the total energy of the adsorption complex, the photocatalyst slab, and the isolated molecule, respectively. The Gibbs free energies ΔG were computed at 298.15 K using the VASPKIT tool, based on the equation: $G = E_{DFT} + E_{ZPE} - T_S$, where E_{DFT}, E_{ZPE}, and T_S denote the electronic energy, zero-point energy, and entropy contribution, respectively [48].

3. Results and discussions

3.1. Characterizations of the prepared catalysts

To explore the phase structure of the TO, BTO-1, BTO-2, and BTO-3 catalysts, the X-ray diffraction measurement was conducted, and the diffraction peaks of the materials with the corresponding standard cards are exhibited in Fig. 1. There are six diffraction peaks of as-synthesized catalysts located at 25.3, 37.8, 48.0, 53.9, 55.1, and 62.7 °, which could be assigned to the (101), (004), (200), (105), (211), and (204) crystal facets of anatase TiO_2 (JCPDS No.21-1272), respectively. Besides, the additional eight prominent diffraction peaks of series BTO-X (X = 1, 2, and 3) catalysts were detected at 22.5, 27.2, 37.9, 39.6, 48.7, 55.6, 62.2, and 64.5 °, which are assigned to the (003), (012), (104), (202), (024), (116), and (122) crystal facets of metallic Bi (JCPDS No.44-1246), respectively. It indicates that the materials consisting of metallic Bi and anatase TiO_2 were successfully synthesized.

The surface micromorphology of TO, BTO-1, BTO-2, and BTO-3 catalysts were further investigated by SEM and TEM. As shown in Fig. 2a and Fig. S1a, the as-synthesized TO catalyst appeared with the microsphere structure, which the diameter is approximately 4.5 μm. And its rough surface is composed of irregular TiO_2 crystal particles (Fig. 2b and Fig. S1b-c). As shown in Fig. 2c-h, the metallic Bi modified TiO_2 catalysts still retain the microsphere structure. It is observed that the diameter of series BTO-X (X = 1, 2, and 3) microsphere is gradually increased from approximately 5 to 7.5 μm with the precursor dosage increasing of metallic Bi. Significantly, the introduction of Bi source directly affects the surface roughness of the synthesized catalysts, and the more metallic Bi loaded on the surface of TiO_2 made the rougher of the materials' surface significantly. As shown in TEM images of Fig. 2i-l, the surface of BTO-2 catalyst presents a flocculent TiO_2 crystal layer,

which is completely different from the surface of the original TiO_2 (Fig. S1b-c). Moreover, the metallic Bi nanoparticles ($\Phi \approx 50$ nm) are uniformly dispersed in the flocculent TiO_2 crystal layer. It infers that the formed flocculent crystal layers on the surface of the TiO_2 microsphere are caused by the process of in-situ introduction of metallic Bi during the material synthesis. And the flocculent crystal layers can undoubtedly increase the specific surface area of the catalyst, which is beneficial to the adsorption and activation of the reactants.

The N_2 adsorption-desorption isotherms and corresponding pore size distribution curves of TO, BTO-1, BTO-2, and BTO-3 catalysts are shown in Fig. S2. All the catalysts show the type IV isotherm (Brunauer-Deming-Deming-Teller classification), indicating that the mesopores exist in the as-synthesized catalysts. The Table S1 exhibits that the specific surface areas are 57.8, 68.5, 99.2, and 58.3 m^2 g^{-1} of TO, BTO-1, BTO-2, and BTO-3 catalysts, respectively. The specific surface areas show a volcanic change with the dosage increase of Bi resources. The decrease of the specific surface area at BTO-3 catalysts with minimum average pore volume (0.18 cm^3 g^{-1}) is attributed to the blockage of the surface pores caused by the stacking of metallic Bi. The mesopores are further confirmed by the pore size distribution curve, in which the main pore diameter of the TO catalyst is 12.31 nm, while the main pore diameter of series BTO catalysts is approximately 3 nm. The BTO-2 catalyst possesses the maximum specific surface area (99.2 m^2 g^{-1}) and the largest pore volume (0.26 cm^3 g^{-1}). It infers that the BTO-2 catalyst is favorable to adsorbing the reactants (CO_2 and H_2O), and its large pore volume is beneficial to the mass transfer process of intermediates.

The light absorption properties of as-synthesized TO, BTO-1, BTO-2, and BTO-3 catalysts were recorded by the UV-Vis diffuse reflectance spectra (Fig. 3a), and the corresponding band gaps of catalysts were evaluated by the tangent slope of Tauc plot (Fig. 3b). It observed that the light absorption of the metallic Bi modified TiO_2 microsphere catalysts in the visible light range is significantly improved compared with the original TiO_2. It may benefit from the localized surface plasmon resonance effect of metallic Bi. Moreover, the absorption edges gradually redshift and the visible light absorption intensity of BTO catalysts increases with the amount of the metallic Bi precursor. It demonstrates that the localized surface plasmon resonance effect of metallic Bi nanoparticles is contributed to the visible absorption of TiO_2 based material. The estimated band gaps of TO, BTO-1, BTO-2, and BTO-3 catalysts are 2.96, 2.81, 2.52, and 2.38 eV, respectively. It indicates that the band gaps are affected by the introduced metallic Bi. In addition, the valence band XPS spectra and Mott-Schottky plot were further analyzed to study the energy band position of as-synthesized catalysts. As shown in Fig. 3c, the evaluated flat band potentials of the TO catalyst is 0.37 V versus the Ag/AgCl electrode, which is 0.98 V versus the Normal Hydrogen Electrode (NHE) (Eq. 3). The results of valence band XPS spectra (Fig. 3d) shows that the energy gap between the Fermi level (E_f) and valence band (VB) of TO catalyst is evaluated to be 1.38 eV. As an n-type semiconductor, the Fermi level of TiO_2 is equal to flat band potential [49], thus the valence band position of the TO catalyst is calculated to be 2.36 V. According to the band gap of TiO_2, its conduction band position is further calculated to be -0.60 V, which satisfies the redox potential of CO_2 being reduced to CO (-0.53 V vs. NHE) and CH_4 (-0.24 V vs. NHE).

$$E_{NHE} = E_{AgCl} + E_{AgCl}^0 + 0.059pH \tag{3}$$

Where the E_{AgCl}^0 value is 0.197 V, and the pH value is 7.0.

To analyze the surface chemical environment, the elemental composition, and the corresponding atomic valence states of TO, BTO-1, BTO-2, and BTO-3 catalysts, the X-ray photoelectron spectroscopy (XPS) was conducted. As shown in Fig. S3 and Fig. 4a–c, the survey of total elements and the high-resolution XPS characteristic peaks of O, Ti, and Bi elements were investigated. The O 1 s characteristic peaks of the TO and BTO catalysts could be divided into two and three sub-peaks,
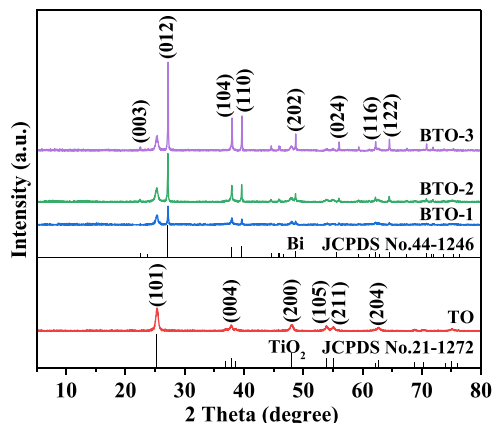

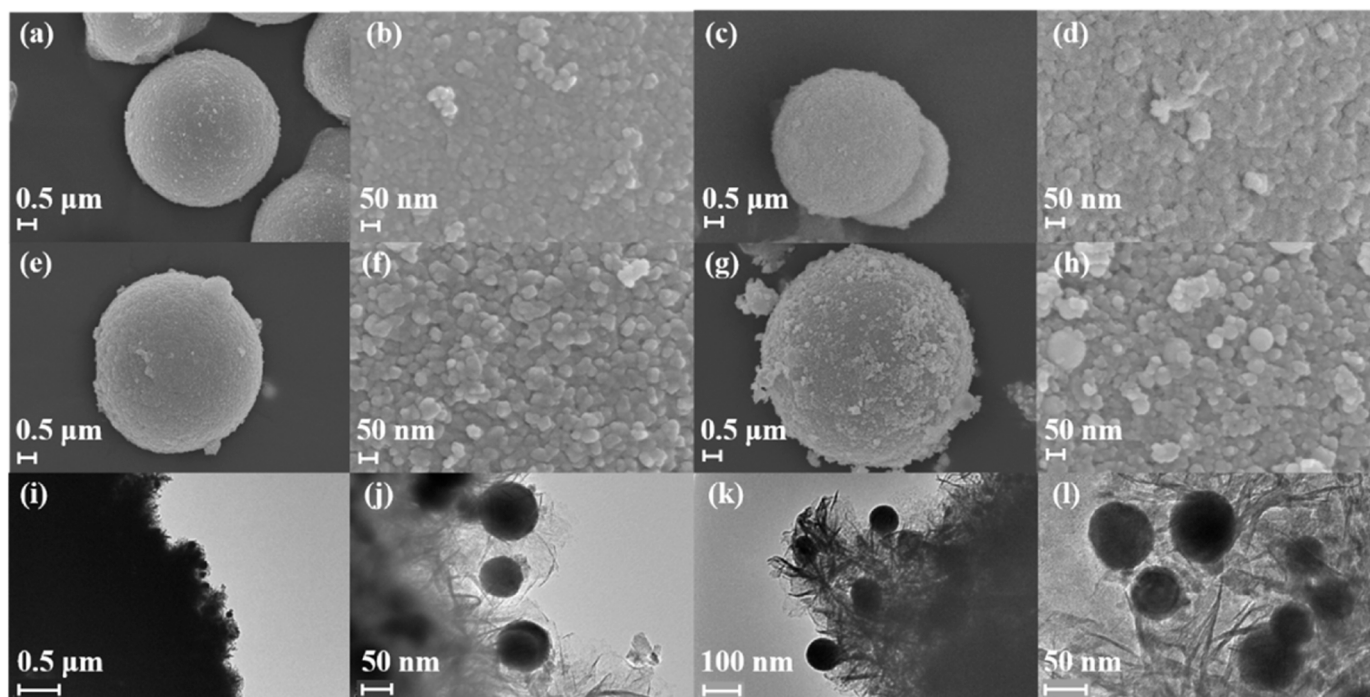**Fig. 1.** The XRD patterns of TO, BTO-1, BTO-2, and BTO-3 catalysts.

Fig. 2. SEM images of TO (a, b), BTO-1 (c, d), BTO-2 (e, f), and BTO-3 (g, h); TEM images of BTO-2 (i-l).
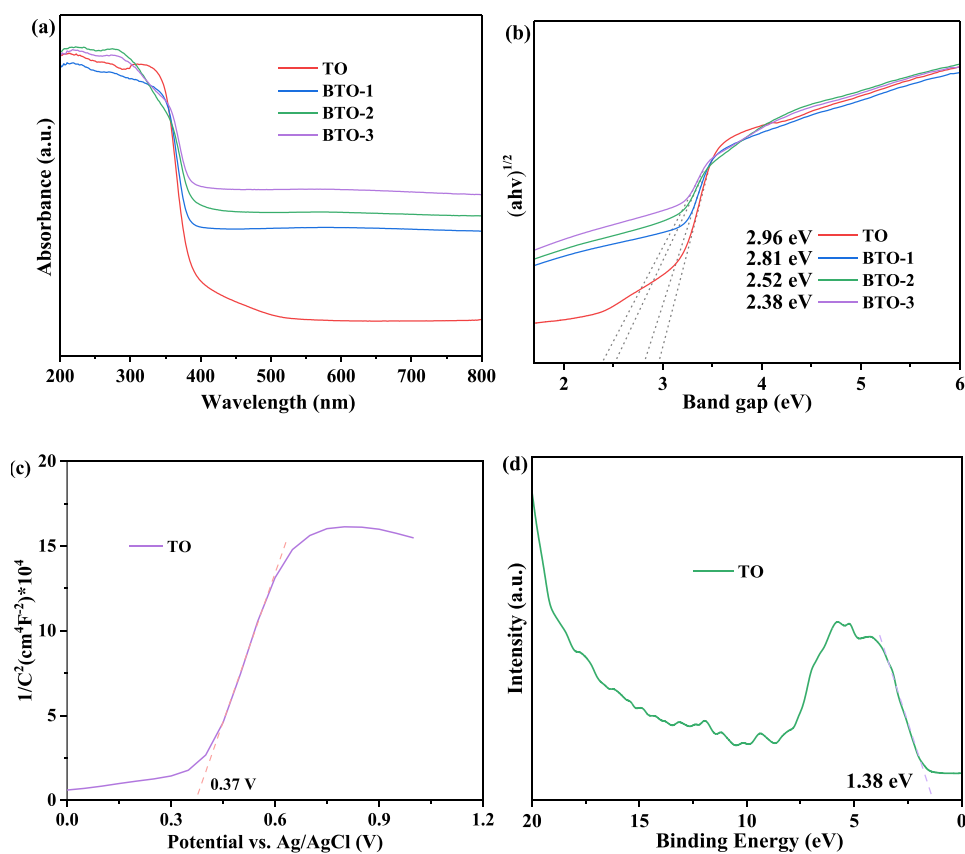

Fig. 3. The UV-Vis DRS (a) and the corresponding band gaps (b) of TO, BTO-1, BTO-2, and BTO-3 catalysts; The Mott-Schottky plots (c) and the valence-band XPS spectra (d) of TO catalyst.

respectively. The sub-peaks at 529.6 and 530.2 eV are assigned to the Bi-O and Ti-O bonds of lattice oxygen in as-synthesized materials. The XPS characteristic peak at 531.7 eV could be assigned to the O-H bond of the surface adsorbed H_2O/OH^- over the TO and series BTO catalysts. Notably, the integral areas (Table S2) of Bi-O bonds are increased and the integral areas of the Ti-O bonds are decreased, as the more dosage Bi
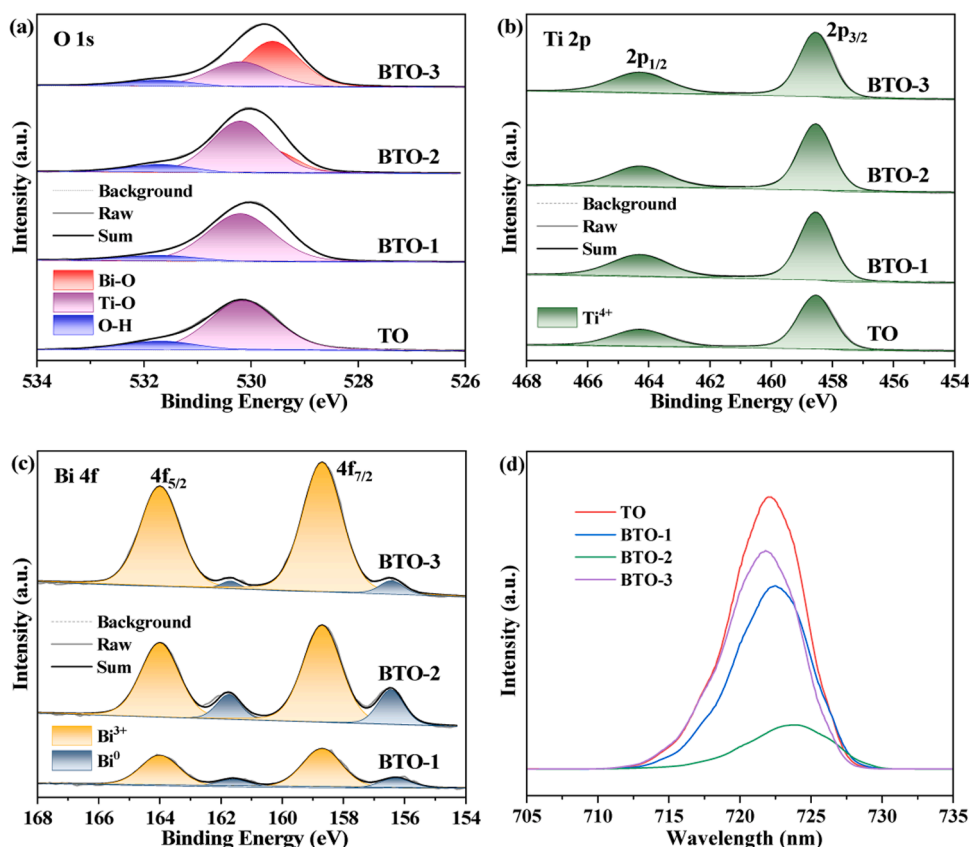
Fig. 4. XPS spectra of O 1s (a), Ti 2p (b), Bi 4f (c) and the PL spectra of TO, BTO-1, BTO-2, and BTO-3 catalysts.

resources participated into the synthesis of BTO catalysts. It demonstrates that the introduced Bi resources are distributed on the surface of TiO_2 microsphere, moreover, the Bi atoms and Ti atoms are both exposed. The integral areas statistics of O-H bonds on surface of different catalysts indicate that the exposure decrease of surface titanium atoms weakened the H_2O/OH^- adsorption capacity. It infers that the titanium atoms are the main active sites for water splitting. As shown in Fig. 4b, the Ti 2p characteristic peaks are detected at 458.54 eV (Ti $2p_{1/2}$) and 464.27 eV (Ti $2p_{3/2}$). And the corresponding peak areas (Table S3) gradually decreased with the Bi resources increasing, indicating that the introduced Bi element resources occupied the partial surface of TiO_2.

As shown in Fig. 4c, the Bi $4f_{7/2}$ and Bi $4f_{5/2}$ of the Bi 4f characteristic peaks could be divided into two sub-peaks, respectively. In which the sub-peaks at 156.3 and 161.6 eV are attributed to the Bi^0 species, the sub-peaks at 158.7 and 164.0 eV are attributed to the Bi^{3+} species. For the reason that the reducing solvent (Isopropanol) was used in the synthesis of series BTO catalysts, hence the metallic Bi were emerged and adhered on the surface of TiO_2. As exhibited in Table S4, it is reasonable to that the integral area of total Bi species (Bi^{3+} and Bi^0) and the Bi^{3+} species are increased with using more Bi resources. Especially, the integral area of Bi^0 species varied with the increasing of metallic Bi loading, the percentages of Bi^0 species in BTO catalysts were expressed by $S^0_{\uparrow Bi}/S^{4+}_{\uparrow Ti}$, and the values of BTO-1, BTO-2 and BTO-3 are 1.94 %, 5.60 % and 1.70 %, respectively. The metallic Bi nanoparticles possesses the largest proportion in BTO-2 catalyst. It indicates that the precipitation amount of metallic Bi is responding to the suitable concentration of Bi resources in a specific reducing solvent. Obviously, the exposure of abundant metallic Bi possesses a strong LSPR effect on the TiO_2 interface and is beneficial to improve the photoelectric performance of the BTO catalyst.

Furthermore, the photoluminescence (PL) spectra (Fig. 4d) were carried on to study the separation efficiency of photogenerated electron-hole pairs in as-synthesized TO, BTO-1, BTO-2, and BTO-3 catalysts. The TO catalyst emitted strong PL spectra under light excitation, while the metallic Bi modified TiO_2 catalysts emitted gradually weaken PL spectra with the amount of the metallic Bi increasing. And the BTO-2 catalyst with the largest metallic Bi load emitted the weakest PL spectra. It indicates the highly efficient separation of photogenerated electron-hole pairs in BTO-2 catalyst. Considering that the Fermi level of metallic Bi is − 0.17 V [50], the hot electrons generated by its localized surface plasmon resonance effect are likely to be transferred to the valence band of TiO_2, which is beneficial to facilitate the separation of photogenerated electron-hole pairs of TiO_2.

3.2. Performances of the prepared catalysts

The photocatalytic performance of as-synthesized TO, BTO-1, BTO-2, and BTO-3 catalysts was evaluated by applying them to convert the humid CO_2 (gas-solid phase reaction) under visible light irradiation. The detailed results are exhibited in Table S5. As shown in Fig. 5a–d, the amounts of products CH_4, CO, H_2 and O_2 increased with the visible light illumination time. The formation amounts of CH_4, CO, H_2 and O_2 products over TiO_2 catalysts are 24.00, 22.84, 9.48, and 58.12 μmol g^{-1} under visible light irradiation for 4 h, respectively. The approximative amount of CH_4 and CO products by TiO_2 catalysts indicates the poor product selectivity, which will hinder its practical application. It may be caused by the low visible light absorption and poor electron-hole pairs separation rate of the original TiO_2.

In this works, the series BTO catalysts with metallic Bi modification can photocatalytic humid CO_2 into relatively more CH_4 as well as less CO and H_2 products compared to the original TiO_2. Especially, the CH_4 production increased significantly, which results in the enhancing selectivity of CH_4 as the major reduction product. The yield of the major product CH_4 showed a volcano-type change with the amount increase of
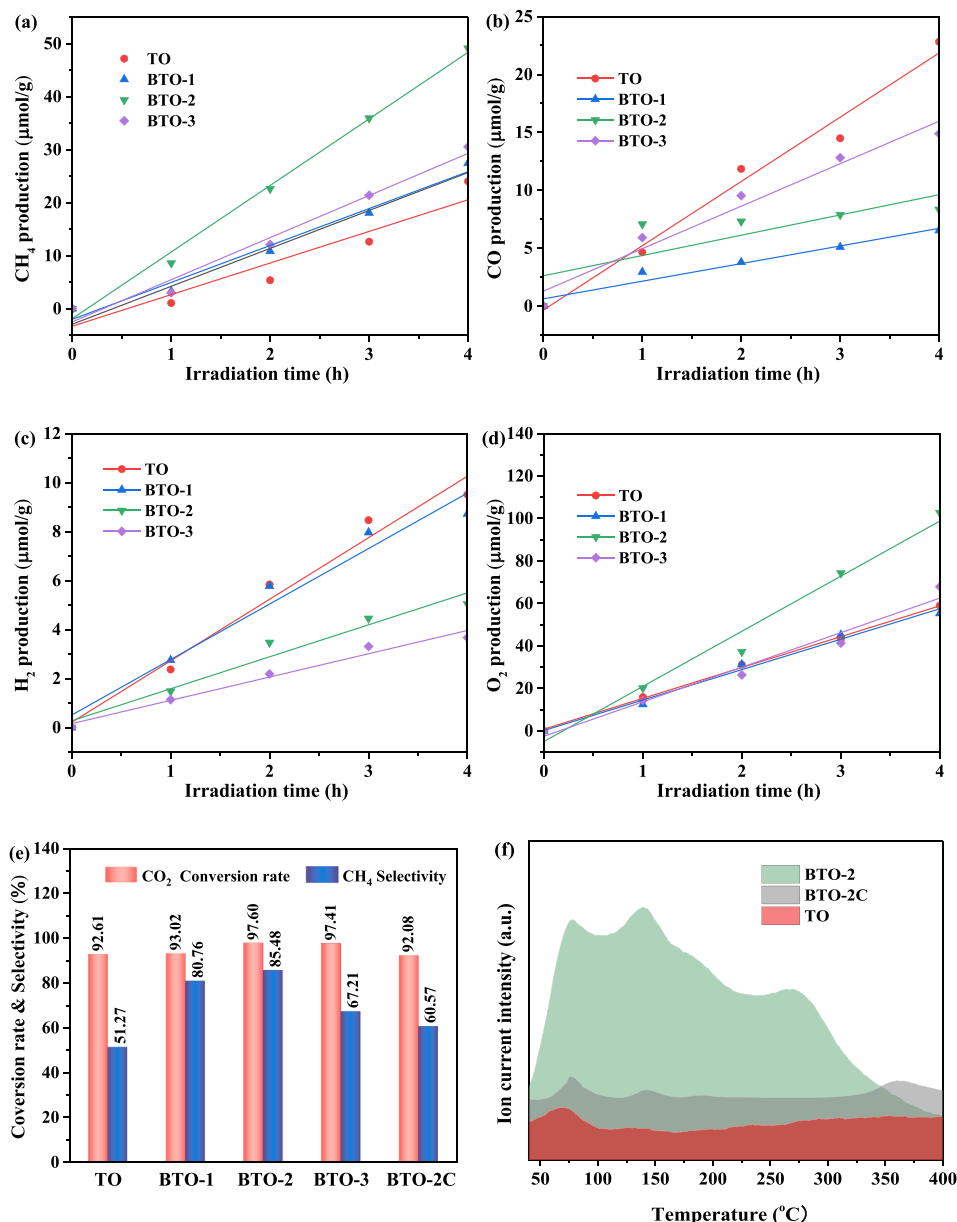
Fig. 5. The formation amount curves of CH_4 (a), CO (b), H_2 (c), and O_2 (d) products vary with time under visible light irradiation over TO and series BTO catalysts; The selectivity of CO_2 reduction and CH_4 product (d) over TO, series BTO and BTO-2 C catalysts; The CO_2-TPD experiments (f) of TO, BTO-2, and BTO-2C catalysts.

the total Bi species (Bi^{3+} and Bi^0), in which the BTO-1 and BTO-3 catalysts with similar CH_4 yields also had a close proportion of metallic Bi, while the BTO-2 catalyst with the maximum proportion of surface metallic Bi produced the maximum amount of CH_4 product. This means that the production of the multi-electron product CH_4 in photocatalytic CO_2 reduction is directly related to the amount of metallic Bi nanoparticles on the surface of the BTO catalyst. The largest amount of CH_4 product is 49.12 μmol g^{-1} over BTO-2 catalyst under 4 h visible light irradiation. Also, the optimal CO_2 conversion rate (97.60 %) and CH_4 product selectivity (85.48 %) both appeared at the BTO-2 catalyst (Fig. 5e). It demonstrates that the LSPR effect of BTO-2 catalyst can induce and enhance the electron-hole pairs separation efficiency, which contributes to the adsorption and activation of CO_2.

To further confirm the crucial role of metallic Bi, the BTO-2 catalyst was oxidized to enable the absence of surface exposed metallic Bi nanoparticles. The basic properties of the deeply oxidized BTO-2 C catalyst are shown in Fig. S4. In comparison with the BTO-2 catalyst, the BTO-2 C catalyst still maintains the microsphere morphology, but its

surface structure is more compact, indicating that the surface metallic Bi is oxidized to bismuth oxide film and covered on the TiO_2 substrate. The phase structure of BTO-2 C was further confirmed by the XRD diffraction spectrum. The metallic Bi diffraction peaks are not detected on BTO-2C, while the diffraction peak of bismuth oxide appeared at 27.9° (201), 32.7° (220), 46.2° (222), 55.5° (421), and so on. The dense bismuth oxide film can not only sharply reduce the specific surface area and average pore volume of the material (Table S1), but also directly affects the photoelectric performance of the catalyst. The visible light absorption intensity of BTO-2 C catalyst is significantly lower than that of the BTO-2 catalyst, and the blueshift of its light absorption band edge widens the corresponding band gap. Also, the photogenerated electron-hole pairs separation rate of BTO-2 C decrease significantly, which will greatly affect its photocatalytic activity. It could be attributed to the lack of metallic Bi, which can enhance visible light absorption and provide hot electrons by the LSPR effect. In this situation, the photocatalytic performance of the BTO-2 C catalyst for CO_2 conversion was greatly reduced (Fig. S5). In particular, the yield (Table S5) of the product CH_4

dropped from the original 12.28 µmol g^{-1} h^{-1} (BTO-2) to 6.88 µmol g^{-1} h^{-1} (BTO-2C), while the yield of the product CO increased significantly, which greatly reduced the product selectivity (Fig. 5e) of the catalyst and inhibited the practical application.

In addition, the detected and stoichiometric O_2 formation rates over the catalysts are listed in Table S6. The actual oxygen amounts are close to the corresponding theoretical oxygen production, indicating that the light-driven CO_2 reduction with H_2O did convert into CH_4, CO, H_2, and O_2 products. To further study the practical application potential of an as-synthesized BTO-2 catalyst, the stability test of photocatalytic CO_2 reduction was conducted. As shown in Fig. S6, the product yield and product selectivity of BTO-2 photocatalytic CO_2 conversion did not change significantly during the five cycle tests. It indicates that the metallic Bi surface-modified TiO_2 microsphere catalyst has the potential for practical application.

3.3. Adsorption and activation properties for CO_2 and H_2O reactants

The adsorption capacity of TO, BTO-2, and BTO-2 C catalysts for CO_2 reactant was investigated by CO_2 temperature-programmed desorption experiments. To exclude the adsorbed impurity gases, the catalyst was pretreated by heat at 200 °C in an N_2 atmosphere. The mixed gas (CO_2 and N_2) with a certain concentration and flow rate passed over the surface of the catalyst for CO_2 saturated adsorption at room temperature, and then pure N_2 was introduced to remove the weakly adsorbed CO_2 on the surface of catalyst. The m/z signal at 44 (CO_2) was continuously recorded in the process of temperature-programmed desorption experiments by Mass spectrum. The result shows that the CO_2 adsorption capacity of catalysts is ranked as BTO-2 > BTO-2 C > TO (Table S7). As shown in Fig. 5f, only one apparent peak (at 70 °C) and the low CO_2 adsorption amount, indicate the non-affinity of TO catalyst to CO_2. There are four adsorption peaks of the BTO-2 catalyst at around 77, 145, 193, and 269 °C, which represent different adsorption

intensities of the BTO-2 catalyst to CO_2. In comparison with the BTO-2 catalyst, even though BTO-2 C had a relatively more stable CO_2 adsorption peak at 363 °C, the adsorption amount of BTO-2 C to CO_2 decreased drastically. This indicates that the presence of metallic Bi greatly increases the adsorption of CO_2 on the BTO-2 catalyst, which is undoubtedly beneficial to the conversion of CO_2.

To insight into the process of photocatalytic CO_2 conversion, the time-varying molecular vibration spectra were continuously recorded by in-situ DRIFTS to trace the surface species of TO and BTO-2 catalysts under dark and visible light irradiation conditions. The various wavenumbers corresponding to vibration characteristic peaks of different species are listed in Table S8. In dark conditions (Fig. 6a), various activated species which are evolved from CO_2 were traced over the surface of TO catalyst. Accompanied by the asymmetric stretching vibration at around 2000–1800 cm^{-1} of C═O bond in carbonyl [51]. The vibration characteristic peak at 1673, 1644, and 1249 cm^{-1} could be assigned to the asymmetric stretching vibration of •CO_2^- species which is derived from the CO_2 accepted an electron [52]. Meanwhile, the HCO_3^- and CO_3^{2-} species are also determined. The vibration characteristic peaks at around 1396 cm^{-1} and 1342 cm^{-1} are assigned to the asymmetric stretching vibration of [CO_3] in HCO_3^- over TO catalyst [53]. The vibration characteristic peaks of CO_3^{2-} species could be confirmed by the symmetrical stretching vibration of [CO_3] at around 1738, 1579/1567, and 1518 cm^{-1} over the TO catalyst [54,55]. They are corresponding to the different adsorption modes of CO_3^{2-} species over TO catalyst, i.e., the chelating-bridged carbonate (c-CO_3^{2-}), bidentate carbonate species (b-CO_3^{2-}), and monodentate carbonate (m-CO_3^{2-}). During the visible light irradiation (Fig. 6b), the wavenumbers of vibration characteristic peaks corresponding to b-CO_3^{2-} species were shifted from 1579/1567 cm^{-1} to 1562/1549 cm^{-1}. It demonstrates that the binding intensity of b-CO_3^{2-} species on the surface of the TO catalyst was weakened by light stimulation. And the wavenumber of vibration characteristic peak corresponding to HCO_3^- species was shifted from 1342 cm^{-1} to 1350 cm^{-1},
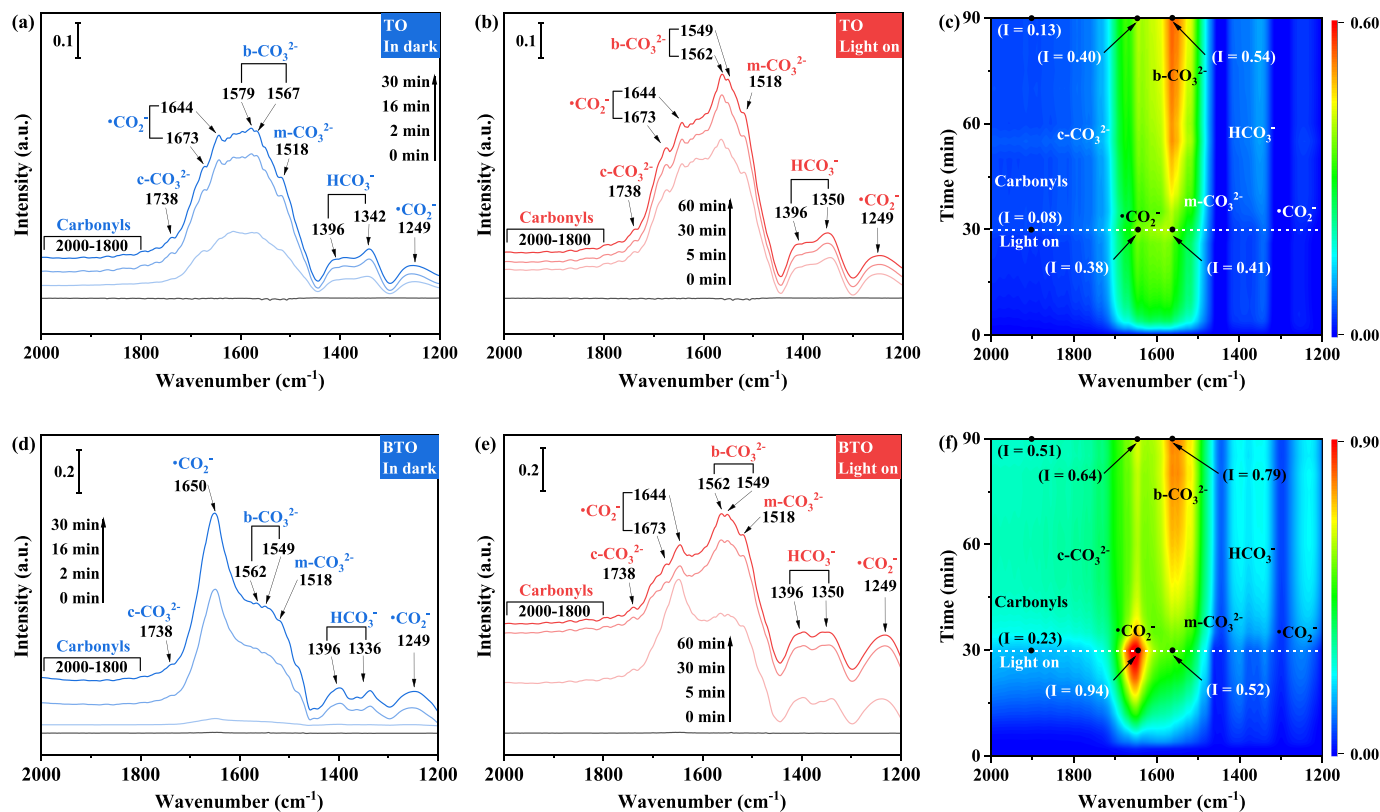

Fig. 6. In-situ DRIFTS of CO_2 and H_2O adsorbed on TO (a, b) and BTO-2 (d, e) catalysts under dark and visible light irradiation conditions as well as the corresponding heatmaps over TO (c) and BTO-2 (f) catalysts.

which indicates that the binding intensity of HCO_3^- species on the surface of the TO catalyst was strengthened by the light stimulation.

As shown in Fig. 6c, the heatmap clearly reflects the time-varying amounts of different adsorbed species on the TO catalyst. Among all the traced species, the b-CO_3^{2-} species accumulated on the surface of the TO catalyst with irradiation time, while the amounts of other species had no significant change. The intensity of b-CO_3^{2-} species increased from 0.41 to 0.54 but its peak shifted to a low wavenumber. It indicated that visible light promotes the accumulation of b-CO_3^{2-} species, but its binding intensity on TO catalysts' surface tends to weaken. In brief, the adsorbed b-CO_3^{2-} species is not conducive to further activating at the surface of TO catalyst under light irradiation. As shown in Fig. 6d-e, the surface species' vibration peak curves of the BTO catalyst are different from that of the TO catalyst. In dark conditions, the wavenumber at 1650 cm^{-1} appeared a sharp peak which could be assigned to the asymmetric stretching vibration of $\bullet CO_2^-$ species. Especially, the wavenumber of HCO_3^- species at 1336 cm^{-1} was shifted to 1350 cm^{-1} after light irradiation. It indicates that the binding intensity of HCO_3^- species on the surface of the BTO catalyst was strengthened by light stimulation.

The heatmap (Fig. 6f) reveals that all the adsorbed species on the BTO catalyst respond to the visible light immediately. The vibration intensity of c-CO_3^{2-} species, m-CO_3^{2-} species, b-CO_3^{2-} species as well as HCO_3^- species increased significantly, especially the vibration intensity of b-CO_3^{2-} species increased from 0.52 to 0.79. It demonstrates that abundant free carbonates and bicarbonates in a moist CO_2 atmosphere were anchored on the surface of the BTO catalyst after the photo-generated electrons migrate to the interface. Accompanied by the vibration peak strength of Carbonyls from 0.23 to 0.51, the vibration peak intensity of $\bullet CO_2^-$ species at 1673/1644 cm^{-1} decreased from 0.96 to 0.64 while that at 1249 cm^{-1} increased. It indicates that the $\bullet CO_2^-$ species are continuously generated and consumed under visible light conditions. And the CO_3^{2-} species and HCO_3^- species could also be transformed from $\bullet CO_2^-$ species in theory.

To evaluate the electron transfer direction inner BTO catalyst, the visualizable charge difference distribution between metallic Bi and TiO_2 was calculated by DFT calculation (Fig. S7a). It indicates that the BTO catalyst trends to localize electrons at the interface from the electrons-enriched metallic Bi. The result is in line with the analysis of energy band position, thus more electrons possess the chance to participate in the surface reduction reaction. Furthermore, the adsorption structures of reactants and key intermediates were optimized over TO and BTO catalysts (Fig. S7b-o), respectively. The calculated Bader charge of adsorbed H_2O^* and CO_2^* molecules over TO catalyst are 0.01 e and 0.04 e, and the corresponding Bader charge that over BTO catalyst are − 0.02 e and 0.15 e. In comparison with the CO_2^* molecule over TO catalyst, the CO_2^* molecule over BTO catalyst has accepted more electrons. And the H_2O^* molecule over BTO catalyst can donate electrons instead of acceptance, which demonstrates that the BTO catalyst holds an advantageous surface surrounding for the reaction of CO_2 and H_2O molecules.

In addition, the Bader charge of adsorbed CO_3^{2-} and HCO_3^- species over BTO catalyst are 1.28 e and 0.71 e, which are large than the Bader charge of adsorbed CO_3^{2-} (1.26 e) and HCO_3^- (0.67 e) species over TO catalyst, respectively. Moreover, the Bader charge of adsorbed CO^* (0.51 e) and HCO^* (0.55 e) species over BTO catalyst also accepted more electrons than the Bader charge of adsorbed CO^* (0.35 e) and HCO^* (0.51 e) species over TO catalyst, respectively. It indicates that the key intermediates of photocatalytic CO_2 conversion are conducive to being adsorbed and activated at the surface of metallic Bi modified TiO_2 catalysts. According to the optimized structure, the bond lengths and bond angles of adsorbed H_2O^* and CO_2^* were marked as shown in Fig. 7a. The bond lengths of H_2O^* over the TO and BTO catalysts both have no obvious change, but its bond angle broadened after optimized over TO catalyst. Combined with the result of the Bader charge, indicating that the H_2O molecule trend to gather electrons from the TO catalyst, hence the H_2 as the by-product of CO_2 photoconversion may be generated at the surface of the original TO catalyst easily in comparison with the BTO

catalyst. Noteworthiness, the bond lengths are lengthened and bond angles are broadened of adsorbed CO_2^* after optimization at the surfaces of TO and BTO catalysts. It is worth noting that the bond length of CO_2^* over BTO catalyst is longer than that over TO catalyst. During the CO_2 reduction reaction, the electrons gather at CO_2 molecule lengthened its bond lengths, which is conducive to the hydrodeoxygenation of CO_2. It further demonstrates that the BTO catalyst holds an advantageous surface surrounding the reaction of CO_2 and H_2O molecules.

The images of electron localized function are exhibited in Fig. 7b-c. It observed that the CO_2^*, CO_3^{2-} and HCO_3^- species all adsorbed at a titanium atom of TO catalyst with the bidentate chelation form. The CO_2^* and CO_3^{2-} species also bidentate chelate on a titanium atom of the BTO catalyst, and the HCO_3^- species adsorbed at two titanium atoms with the bridged chelation form. It indicates that the stable adsorption of the CO_2^*, CO_3^{2-} and HCO_3^- species, which is conducive to further reaction. Especially, the CO_2 molecule bonded at the titanium atom on the BTO catalyst by the mixed (carbon and oxygen) atoms ligand, which provides another oxygen atom the advantage to escape after catching the hydrogen proton. As above, the in-situ DRIFTS combines with DFT calculation, resulting that the CO_2^*, CO_3^{2-} and HCO_3^- species over BTO catalyst are sensitive to visible light. The $\bullet CO_2^-$ species over BTO catalyst could be converted to CO_3^{2-} and HCO_3^-, or hydrodeoxygenation directly under visible light irradiation.

3.4. Mechanism of CO_2 photoreduction

Based on the key intermediate species [CO_2^*, $COOH^*$, CO^* and HCO^* /CO (g)] of the CO_2 reduction reaction, the relative reaction energies of each species were calculated by DFT calculation (Fig. 8a). The energy gaps between CO_2^* and $COOH^*$ over TO and BTO slabs are 0.18 and 0.15 eV, respectively. It demonstrates that the adsorbed CO_2 molecules could catch a hydrogen proton and be converted to $COOH^*$ species after suffering from hot electron injection ($CO_2^* + H^+ + e^- \rightarrow COOH^*$), or the $COOH^*$ can derived from other forms of activated CO_2 i. e., CO_3^{2-} and HCO_3^- ($CO_3^{2-} + 3 H^+ + e^- \rightarrow COOH^* + H_2O$; $HCO_3^- + 2 H^+ + e^- \rightarrow COOH^* + H_2O$). It is worth noting that the lower energy gap indicates that the relatively easy production of $COOH^*$ occurred on the surface of BTO catalyst in comparison with that on TO catalyst. Furthermore, the hydrodeoxygenation process of $COOH^*$ species on the surfaces of both TO and BTO slabs can be carried out spontaneously, cause of the decreased reaction energies from $COOH^*$ to CO^* species. The stable adsorption of CO^* is the key to its further hydrodeoxygenation, and its desorption will terminate the reduction process and make the final product of the CO_2 photoreduction reaction be gaseous CO molecule. The result shows that the transformation from CO^* to CO (g) or HCO^* species both require extra energy. And, on the surface of TO and BTO catalysts, the formation of HCO^* needs less energy than that of CO (g). The further hydrodeoxygenation of HCO^* species leads to the formation of CH_4 product. Hence, the dominant product of photocatalytic CO_2 reduction by TO and BTO catalysts is CH_4 instead of CO product. Notably, the required extra energy of CO^* -to-HCO^* by BTO catalysis is lower than that by TO catalysis. It demonstrates the priority to selectively convert CO_2 into CH_4 by BTO catalysis in theory.

According to the analysis of in-situ DRIFTS and DFT calculation, the mechanism of CO_2 photoconversion over BTO catalyst was proposed. As shown in Fig. 8b, the reactant CO_2 adsorbed at the surface of the TiO_2 component of BTO catalysts directly, or dissolved in water vapor and captured by the catalyst surface in the form of CO_3^{2-} and HCO_3^- species. Meanwhile, ionized state ions of hydrogen and hydroxide are surrounded by the reactant and adsorbed on the surface of the catalyst. The visible light as the energy source stimulates the process of electron-hole pairs separation in semiconduction material, and the metallic Bi with light-induced LSPR effect donates hot electrons to the TiO_2 component. The hot electrons derived from metallic Bi were injected into the valence band of TiO_2, which inhibited the back migration and vanishment of
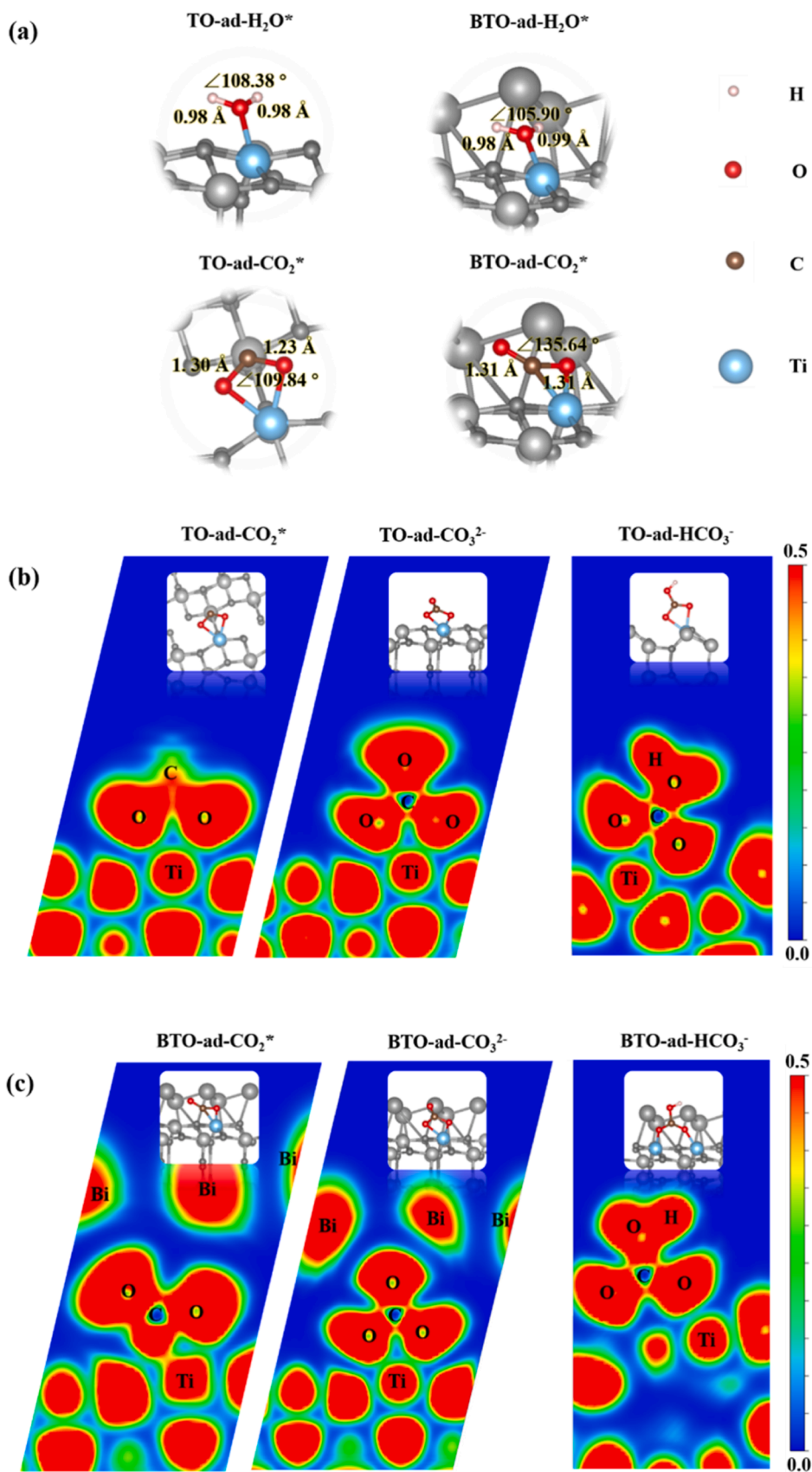
Fig. 7. The Bader charge calculation (a) of H_2O and CO_2* over TO and BTO catalysts; The electronic location function of CO_2*, CO_3^{2-} and HCO_3^- species over TO (b) and BTO (c) catalysts.
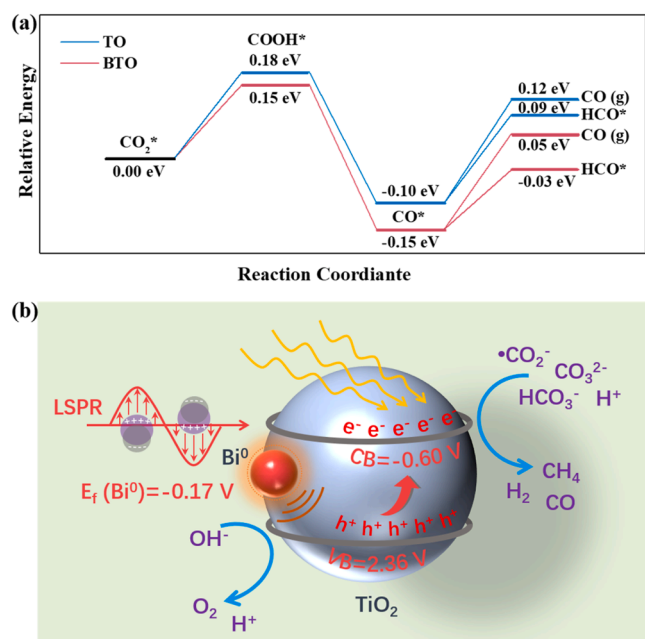
Fig. 8. The calculated free energy of the main reaction in photocatalytic CO_2 reduction (a) over TO and BTO catalysts, and the revolution mechanism (b) of photocatalytic CO_2 reduction over BTO catalyst under visible light conditions.

photoelectrons in TiO_2. Thus, abundant energetic electrons could be transited to the surface of the catalyst to participate in the CO_2 reduction reaction. On the conduction band of TiO_2, the activated CO_2 as the major reactant could be converted to CH_4 and CO. Meanwhile, the hydrogen and oxygen production of the two semi-reactions of H_2O molecular decomposition occur at the conduction and valence band edges of TiO_2 component, respectively.

4. Conclusion

In this works, the TiO_2 microsphere catalysts with metallic Bi nanoparticles modification were synthesized by one-pot solvothermal method. The inherent negative conduction band edge of TiO_2 supplies advantageous redox potential for the CO_2 conversion reaction. And, the visible light-harvesting ability was enhanced by the surface metallic Bi nanoparticles. Significantly, the recombination process of light stimulated electron-hole pairs could be inhibited by the metallic Bi caused LSPR effect which provided hot electrons to vanish the partial holes at the valence band of TiO_2. Thus, abundant high-energy electrons can transfer to participate in the surface reduction reaction, resulting in the efficient photocatalytic CO_2 conversion over metallic Bi modified TiO_2 microsphere catalysts. Especially, the optimized BTO-2 catalyst exhibited a CH_4 production amount of 49.12 μmol g^{-1} and CH_4 selectivity of 85.48 % under visible light irradiation for 4 h. The analysis of in-situ DRIFTS clearly reveals that the $\bullet CO_2^-$ species are heavily accumulated on the optimized BTO catalyst, and its dynamic generation and consumption under visible light conditions represent the continuous activation and conversion of CO_2. The DFT calculation results validated that the superior surface of BTO catalyst adsorbs and activates CO_2 with the mixed (carbon and oxygen) atoms ligand mode. It is conducive to the hydrodeoxygenation process of CO_2^* -to-HCO* , which promote the selective conversion of CO_2 into CH_4. This work supplies a reference to design and insight into the efficient photocatalyst.

CRediT authorship contribution statement

Jing Xiong: Conceptualization, Formal analysis, Funding acquisition, Writing – review & editing. **Wenjie He:** Conceptualization, Data

curation, Investigation, Methodology, Writing – original draft, Writing – review & editing, Validation, Visualization. **Yingli Wang:** Validation. **Zhiling Tang:** Validation. **Hui Xu:** Supervision, Writing – review & editing. **Xiong Wang:** Validation. **Jian Liu:** Supervision, Writing – review & editing. **Zhen Zhao:** Supervision, Writing – review & editing. **Yuechang Wei:** Conceptualization, Data curation, Formal analysis, Funding acquisition, Project administration, Resources, Software, Supervision, Writing – review & editing.

Declaration of Competing Interest

The authors declare that they have no known competing financial interests or personal relationships that could have appeared to influence the work reported in this paper.

Data availability

Data will be made available on request.

Appendix A. Supporting information

Supplementary data associated with this article can be found in the online version at doi:10.1016/j.apcatb.2023.123651.

References

[1] M. Erans, E.S. Sanz-Pérez, D.P. Hanak, Z. Clulow, D.M. Reiner, G.A. Mutch, Direct air capture: process technology, techno-economic and socio-political challenges, Energy Environ. Sci. 15 (2022) 1360–1405, https://doi.org/10.1039/D1EE03523A.

[2] R. Castro-Muñoz, M.Z. Ahmad, M. Malankowska, J. Coronas, A new relevant membrane application: CO_2 direct air capture (DAC), Chem. Eng. J. 446 (2022), 137047, https://doi.org/10.1016/j.cej.2022.137047.

[3] W.A. Algozeeb, P.E. Savas, Z. Yuan, Z. Wang, C. Kittrell, J.N. Hall, W. Chen, P. Bollini, J.M. Tour, Plastic waste product captures carbon dioxide in nanometer pores, ACS Nano 16 (2022) 7284–7290, https://doi.org/10.1021/acsnano.2c00955.

[4] A. Hassani, P. Eghbali, F. Mahdipour, S. Wacławek, K. Lin, F. Ghanbari, Insights into the synergistic role of photocatalytic activation of peroxymonosulfate by UVA-LED irradiation over $CoFe_2O_4$-rGO nanocomposite towards effective Bisphenol A degradation: Performance, mineralization, and activation mechanism, Chem. Eng. J. 453 (2023), 139556, https://doi.org/10.1016/j.cej.2022.139556.

[5] W. Cui, J.Y. Li, F. Dong, Optimizing the gas-solid photocatalytic reactions for air purification, ACS EST Eng. 2 (2022) 1103–1115, https://doi.org/10.1021/acsestengg.1c00503.

[6] J. Peng, F. Deng, H. Shi, Z. Wang, X. Li, J. Zou, X. Luo, Target recognition and preferential degradation of toxic chemical groups by innovative group-imprinted photocatalyst with footprint cavity, Appl. Catal. B: Environ. 340 (2024), 123179, https://doi.org/10.1016/j.apcatb.2023.123179.

[7] Q. You, C. Zhang, M. Cao, B. Wang, J. Huang, Y. Wang, S. Deng, G. Yu, Defects controlling, elements doping, and crystallinity improving triple-strategy modified carbon nitride for efficient photocatalytic diclofenac degradation and H_2O_2 production, Appl. Catal. B: Environ. 321 (2023), 121941, https://doi.org/10.1016/j.apcatb.2022.121941.

[8] Y. Fu, M. Tan, Z. Guo, D. Hao, Y. Xu, H. Du, C. Zhang, J. Guo, Q. Li, Q. Wang, Fabrication of wide-spectra-responsive NA/NH2-MIL-125(Ti) with boosted activity for Cr(VI) reduction and antibacterial effects, Chem. Eng. J. 452 (2023), 139417, https://doi.org/10.1016/j.cej.2022.139417.

[9] H. Li, M. Xia, B. Chong, H. Xiao, B. Zhang, B. Lin, B. Yang, G. Yang, Boosting photocatalytic nitrogen fixation via constructing low-oxidation-state active sites in the nanoconfined spinel iron cobalt oxide, ACS Catal. 12 (2022) 10361–10372, https://doi.org/10.1021/acscatal.2c02282.

[10] M. Lu, M. Zhang, J. Liu, Y. Chen, J. Liao, M. Yang, Y. Cai, S. Li, Y. Lan, Covalent organic framework based functional materials: important catalysts for efficient CO_2 utilization, Angew. Chem. Int. Ed. 61 (2022), e202200003, https://doi.org/10.1002/anie.202200003.

[11] Z. Tang, W. He, Y. Wang, Y. Wei, X. Yu, J. Xiong, X. Wang, X. Zhang, Z. Zhao, J. Liu, Ternary heterojunction in rGO-coated Ag/Cu2O catalysts for boosting

selective photocatalytic CO_2 reduction into CH_4, Appl. Catal. B: Environ. 311 (2022), 121371, https://doi.org/10.1016/j.apcatb.2022.121371.

[12] R. Yang, Y. Fu, H. Wang, D. Zhang, Z. Zhou, Y. Cheng, X. Meng, Y. He, Z. Su, ZIF-8/ covalent organic framework for enhanced CO_2 photocatalytic reduction in gas-solid system, Chem. Eng. J. 450 (2022), 138040, https://doi.org/10.1016/j.cej.2022.138040.

[13] N. Li, X. Chen, J. Wang, X. Liang, L. Ma, X. Jing, D. Chen, Z. Li, ZnSe nanorods-CsSnCl$_3$ perovskite heterojunction composite for photocatalytic CO_2 reduction, ACS Nano 16 (2022) 3332–3340, https://doi.org/10.1021/acsnano.1c11442.

[14] L. Xiong, Y. Hu, Y. Wang, W. Dong, X. Zhang, K. Zhang, T. Wang, J. Shen, Y. Yang, S bridging active centers coordination with oxygen vacancy of metastable blue WO_3 for efficient C-C coupling and highly selective photoconversion CO_2 to ethylene, Appl. Catal. B: Environ. 340 (2024), 123263, https://doi.org/10.1016/j.apcatb.2023.123263.

[15] W. He, Y. Wei, J. Xiong, Z. Tang, W. Song, J. Liu, Z. Zhao, Insight into reaction pathways of CO_2 photoreduction into CH_4 over hollow microsphere Bi$_2$MoO$_6$-supported Au catalysts, Chem. Eng. J. 433 (2022), 133540, https://doi.org/10.1016/j.cej.2021.133540.

[16] X. Wang, J. Jiang, L. Yang, Q. An, Q. Xu, Y. Yang, H. Guo, Enhanced piezoelectric polarization by subtle structure distortion to trigger efficient photocatalytic CO$_2$RR, Appl. Catal. B: Environ. 340 (2024), 123177, https://doi.org/10.1016/j.apcatb.2023.123177.

[17] G. Ren, S. Liu, Z. Li, H. Bai, X. Hu, X. Meng, Highly selective photocatalytic reduction of CO_2 to CO over Ru-modified Bi$_2$MoO$_6$, Sol. RRL 6 (2022), 2200154, https://doi.org/10.1002/solr.202200154.

[18] Y. Xu, M. Zhang, J. Long, W. Dai, P. Wang, L. Yang, J. Zou, X. Luo, Co single atom modulating the secondary coordination environment of Bi sites for boosting the adsorptive and catalytic capacity during CO_2 photoreduction, Appl. Catal. B: Environ. 340 (2024), 123230, https://doi.org/10.1016/j.apcatb.2023.123230.

[19] Y. Kamakura, S. Yasuda, N. Hosokawa, S. Nishioka, S. Hongo, T. Yokoi, D. Tanaka, K. Maeda, Selective CO_2-to-formate conversion driven by visible light over a precious-metal-free nonporous coordination polymer, ACS Catal. 12 (2022) 10172–10178, https://doi.org/10.1021/acscatal.2c02177.

[20] S. Saini, S.R. Khan, N.K. Gour, R.C. Deka, S.L. Jain, Metal-free, redox-neutral, and visible light-triggered coupling of CO_2 with epoxides to cyclic carbonates at atmospheric pressure, Green. Chem. 24 (2022) 3644–3650, https://doi.org/10.1039/D2GC00680D.

[21] M. Cabrero-Antonino, B. Ferrer, H.G. Baldoví, S. Navalón, Toward solar-driven photocatalytic CO_2 methanation under continuous flow operation using benchmark MIL-125(Ti)–NH$_2$ supported ruthenium nanoparticles, Chem. Eng. J. 445 (2022), 136426, https://doi.org/10.1016/j.cej.2022.136426.

[22] J. Li, C. He, N. Xu, K. Wu, Z. Huang, X. Zhao, J. Nan, X. Xiao, Interfacial bonding of hydroxyl-modified g-C$_3$N$_4$ and Bi$_2$O$_2$CO$_3$ toward boosted CO_2 photoreduction: Insights into the key role of OH groups, Chem. Eng. J. 452 (2023), 139191, https://doi.org/10.1016/j.cej.2022.139191.

[23] X. Cheng, J. Wang, K. Zhao, Y. Bi, Spatially confined iron single-atom and potassium ion in carbon nitride toward efficient CO_2 reduction, Appl. Catal. B: Environ. 316 (2022), 121643, https://doi.org/10.1016/j.apcatb.2022.121643.

[24] Z. Yang, Y. Zhang, H. Zhang, J. Zhao, H. Shi, M. Zhang, H. Yang, Z. Zheng, P. Yang, Nitrogen vacancies in polymeric carbon nitrides promote CO_2 photoreduction, J. Catal. 409 (2022) 12–23, https://doi.org/10.1016/j.jcat.2022.03.016.

[25] J. He, X. Wang, S. Lan, H. Tao, X. Luo, Y. Zhou, M. Zhu, Breaking the intrinsic activity barriers of perovskite oxides photocatalysts for catalytic CO_2 reduction via piezoelectric polarization, Appl. Catal. B: Environ. 317 (2022), 121747, https://doi.org/10.1016/j.apcatb.2022.121747.

[26] J. Wang, R. Guo, Z. Bi, X. Chen, X. Hu, W. Pan, A review on TiO$_{2-x}$-based materials for photocatalytic CO_2 reduction, Nanoscale 14 (2022) 11512–11528, https://doi.org/10.1039/D2NR02527B.

[27] Y. Li, Z. Zeng, Y. Zhang, Y. Chen, W. Wang, X. Xu, M. Du, Z. Li, Z. Zou, Deactivation and stabilization mechanism of photothermal CO_2 hydrogenation over black TiO$_2$, ACS Sustain. Chem. Eng. 10 (2022) 6382–6388, https://doi.org/10.1021/acssuschemeng.2c01081.

[28] Y. Li, Z. Ren, Z. Gu, M. Gu, Y. Duan, W. Zhang, K. Lv, Synergistic effect of interstitial C doping and oxygen vacancies on the photoreactivity of TiO$_2$ nanofibers towards CO_2 reduction, Appl. Catal. B: Environ. 317 (2022), 121773, https://doi.org/10.1016/j.apcatb.2022.121773.

[29] J. Park, H. Liu, G. Piao, U. Kang, H. Jeong, C. Janáky, H. Park, Synergistic conversion of CO_2 into C_1 and C_2 gases using hybrid in-doped TiO$_2$ and g-C$_3$N$_4$ photocatalysts, Chem. Eng. J. 437 (2022), 135388, https://doi.org/10.1016/j.cej.2022.135388.

[30] M.S. Choe, S. Choi, H.S. Lee, B. Chon, J.Y. Shin, C.H. Kim, H. Son, S.O. Kang, Sustainable carbon dioxide reduction of the P3HT polymer-sensitized TiO$_2$/Re(I) photocatalyst, ACS Appl. Mater. Interfaces 14 (2022) 50718–50730, https://doi.org/10.1021/acsami.2c09924.

[31] B. Chon, S. Choi, Y. Seo, H.S. Lee, C.H. Kim, H. Son, S.O. Kang, InP-quantum dot surface-modified TiO$_2$ catalysts for sustainable photochemical carbon dioxide reduction, ACS Sustain. Chem. Eng. 10 (2022) 6033–6044, https://doi.org/10.1021/acssuschemeng.2c00938.

[32] Y. Feng, C. Wang, P. Cui, C. Li, B. Zhang, L. Gan, S. Zhang, X. Zhang, X. Zhou, Z. Sun, K. Wang, Y. Duan, H. Li, K. Zhou, H. Huang, A. Li, C. Zhuang, L. Wang, Z. Zhang, X. Han, Ultrahigh photocatalytic CO_2 reduction efficiency and selectivity manipulation by single-tungsten-atom oxide at the atomic step of TiO$_2$, Adv. Mater. 34 (2022), 2109074, https://doi.org/10.1002/adma.202109074.

[33] W. Bi, L. Zhang, H. Jiang, C. Li, Y. Hu, Construction of CuInS$_2$/C/TiO$_2$ hierarchical tandem heterostructures with optimized CO_2 photoreduction under visible light, Chem. Eng. J. 433 (2022), 133679, https://doi.org/10.1016/j.cej.2021.133679.

[34] T. Wang, L. Chen, C. Chen, M. Huang, Y. Huang, S. Liu, B. Li, Engineering catalytic interfaces in Cu$^{\delta+}$/CeO$_2$-TiO$_2$ photocatalysts for synergistically boosting CO_2 reduction to ethylene, ACS Nano 16 (2022) 2306–2318, https://doi.org/10.1021/acsnano.1c08505.

[35] K.M. Kamal, R. Narayan, N. Chandran, S. Popović, M.A. Nazrulla, J. Kovač, N. Vrtovec, M. Bele, N. Hodnik, M.M. Kržmanc, B. Likozar, Synergistic enhancement of photocatalytic CO_2 reduction by plasmonic Au nanoparticles on TiO$_2$ decorated N-graphene heterostructure catalyst for high selectivity methane production, Appl. Catal. B: Environ. 307 (2022), 121181, https://doi.org/10.1016/j.apcatb.2022.121181.

[36] J. Yang, Y. Zhang, X. Xie, W. Fang, G. Cui, Photocatalytic reduction of carbon dioxide to methane at the Pd-supported TiO$_2$ interface: mechanistic insights from theoretical studies, ACS Catal. 12 (2022) 8558–8571, https://doi.org/10.1021/acscatal.2c01519.

[37] H. Huang, R. Shi, Z. Li, J. Zhao, C. Su, T. Zhang, Triphase photocatalytic CO_2 reduction over silver-decorated titanium oxide at a gas-water boundary, Angew. Chem. Int. Ed. 61 (2022), e202200802, https://doi.org/10.1002/anie.202200802.

[38] S. Kang, J. Hwang, rGO-wrapped Ag-doped TiO$_2$ nanofibers for photocatalytic CO_2 reduction under visible light, J. Clean. Prod. 374 (2022), 134022, https://doi.org/10.1016/j.jclepro.2022.134022.

[39] R. Wang, J. Shen, K. Sun, H. Tang, Q. Liu, Enhancement in photocatalytic activity of CO_2 reduction to CH_4 by 0D/2D Au/TiO$_2$ plasmon heterojunction, Appl. Surf. Sci. 493 (2019) 1142–1149, https://doi.org/10.1016/j.apsusc.2019.07.121.

[40] G. Li, Y. Sun, Q. Zhang, Z. Gao, W. Sun, X. Zhou, Ag quantum dots modified hierarchically porous and defective TiO$_2$ nanoparticles for improved photocatalytic CO_2 reduction, Chem. Eng. J. 410 (2021), 128397, https://doi.org/10.1016/j.cej.2020.128397.

[41] M. Zhang, J. Ke, D. Xu, X. Zhang, H. Liu, Y. Wang, J. Yu, Construction of plasmonic Bi/Bismuth oxycarbonate/Zinc bismuth oxide ternary heterojunction for enhanced charge carrier separation and photocatalytic performances, J. Colloid Interface Sci. 615 (2022) 663–673, https://doi.org/10.1016/j.jcis.2022.02.026.

[42] Y. Wang, Z. Bian, L. Zhang, H. Wang, Bi@BiO$_x$(OH)$_y$ modified oxidized g-C$_3$N$_4$ photocatalytic removal of tetracycline hydrochloride with highly effective oxygen activation, J. Hazard. Mater. 427 (2022), 127866, https://doi.org/10.1016/j.jhazmat.2021.127866.

[43] X. Guan, X. Zhang, C. Zhang, R. Li, J. Liu, Y. Wang, Y. Wang, C. Fan, Z. Li, In situ hydrothermal synthesis of metallic Bi self-deposited Bi$_2$SiO$_5$ with enhanced photocatalytic CO_2 reduction performance, Sol. Rrl 6 (2022), 2200346, https://doi.org/10.1002/solr.202200346.

[44] L. Wang, H. Yin, S. Wang, J. Wang, S. Ai, Ni^{2+}-assisted catalytic one-step synthesis of Bi/BiOCl/Bi$_2$O$_2$CO$_3$ heterojunction with enhanced photocatalytic activity under visible light, Appl. Catal. B: Environ. 305 (2022), 121039, https://doi.org/10.1016/j.apcatb.2021.121039.

[45] L. Zhao, Y. Liu, X. Xi, Y. Shen, J. Wang, Y. Liu, Z. Nie, Bi/Bi$_2$O$_3$/WO$_3$ composite: A bifunctional plasmonic heterostructure for detection and degradation pollutions in wastewater, J. Environ. Chem. Eng. 10 (2022), 107643, https://doi.org/10.1016/j.jece.2022.107643.

[46] Z. Zhang, L. Zhou, P.E. Wigen, K. Ounadjela, Angular dependence of ferromagnetic resonance in exchange-coupled Co/Ru/Co trilayer structures, Phys. Rev. B 50 (1994) 6094–6112, https://doi.org/10.1103/PhysRevB.50.6094.

[47] J. Li, S. Yin, F. Dong, W. Cen, Y. Chu, Tailoring active sites via synergy between graphitic and pyridinic N for enhanced catalytic efficiency of a carbocatalyst, ACS Appl. Mater. Interfaces 9 (2017) 19861–19869, https://doi.org/10.1021/acsami.7b04026.

[48] J. Sheng, Y. He, J. Li, C. Yuan, H. Huang, S. Wang, Y. Sun, Z. Wang, F. Dong, Identification of halogen-associated active sites on bismuth-based perovskite quantum dots for efficient and selective CO_2-to-CO photoreduction, ACS Nano 14 (2020) 13103–13114, https://doi.org/10.1021/acsnano.0c04659.

[49] X. Yang, S. Wang, N. Yang, W. Zhou, P. Wang, K. Jiang, S. Li, H. Song, X. Ding, H. Chen, J. Ye, Oxygen vacancies induced special CO_2 adsorption modes on Bi$_2$MoO$_6$ for highly selective conversion to CH_4, Appl. Catal. B: Environ. 259 (2019), 118088, https://doi.org/10.1016/j.apcatb.2019.118088.

[50] W. He, Y. Sun, G. Jiang, Y. Li, X. Zhang, Y. Zhang, Y. Zhou, F. Dong, Defective Bi$_4$MoO$_9$/Bi metal core/shell heterostructure: enhanced visible light photocatalysis and reaction mechanism, Appl. Catal. B: Environ. 239 (2018) 619–627, https://doi.org/10.1016/j.apcatb.2018.08.064.

[51] H. Zhang, Q. Hong, J. Li, F. Wang, X. Huang, S. Chen, W. Tu, D. Yu, R. Xu, T. Zhou, J. Zhang, Isolated square-planar copper center in boron imidazolate nanocages for photocatalytic reduction of CO_2 to CO, Angew. Chem. Int. Ed. 58 (2019) 11752–11756, https://doi.org/10.1002/anie.201905869.

[52] M. Wang, M. Shen, X.X. Jin, J.J. Tian, M.L. Li, Y.J. Zhou, L.X. Zhang, Y.S. Li, J.L. Shi, Oxygen vacancy generation and stabilization in CeO$_{2-x}$ by Cu introduction with improved CO_2 photocatalytic reduction activity, ACS Catal. 9 (2019) 4573–4581, https://doi.org/10.1021/acscatal.8b03975.

[53] X. Li, Y. Sun, J. Xu, Y. Shao, J. Wu, X. Xu, Y. Pan, H. Ju, J. Zhu, Y. Xie, Selective visible-light-driven photocatalytic CO_2 reduction to CH_4 mediated by atomically thin CuIn$_5$S$_8$ layers, Nat. Energy 4 (2019) 690–699, https://doi.org/10.1038/s41560-019-0431-1.

[54] J. Wu, X.D. Li, W. Shi, P.Q. Ling, Y.F. Sun, X.C. Jiao, S. Gao, L. Liang, J.Q. Xu, W.S. Yan, C.M. Wang, Y. Xie, Efficient visible-light-driven CO_2 reduction mediated by defect-engineered BiOBr atomic layers, Angew. Chem. Int. Ed. 57 (2018) 8719–8723, https://doi.org/10.1002/anie.201803514.

[55] S.Q. Zhu, T.H. Li, W.B. Cai, M.H. Shao, CO_2 electrochemical reduction as probed through infrared spectroscopy, ACS Energy Lett. 4 (2019) 682–689, https://doi.org/10.1021/acsenergylett.8b02525.